Review article

Parameter extraction techniques for the analysis and modeling of resistive memories

D. Maldonado [a], S. Aldana [a], M.B. González [b], F. Jiménez-Molinos [a], F. Campabadal [b], J.B. Roldán [a,*]

[a] *Departamento de Electrónica y Tecnología de Computadores, Universidad de Granada, Facultad de Ciencias, Avd. Fuentenueva s/n, 18071 Granada, Spain*
[b] *Institut de Microelectrònica de Barcelona, IMB-CNM (CSIC), Carrer dels Til·lers, s/n. Campus UAB, 08193 Bellaterra, Spain*

A B S T R A C T

A revision of the different numerical techniques employed to extract resistive switching (RS) and modeling parameters is presented. The set and reset voltages, commonly used for variability estimation, are calculated for different resistive memory technologies. The methodologies to extract the series resistance and the parameters linked to the charge-flux memristive modeling approach are also described. It is found that the obtained cycle-to-cycle (C2C) variability depends on the numerical technique used. This result is important, and it implies that when analyzing C2C variability, the extraction technique should be described to perform fair comparisons between different resistive memory technologies. In addition to the use of extensive experimental data for different types of resistive memories, we have also included kinetic Monte Carlo (kMC) simulations to study the formation and rupture events of the percolation paths that constitute the conductive filaments (CF) that allow resistive switching operation in filamentary unipolar and bipolar devices.

1. Introduction

Memristive devices [1–3] are under scrutiny by the scientific community due to their potential in applications of most interest in the electronics landscape, such as non-volatile memory ICs [4–7], neuromorphic computing [8–18] and hardware cryptography [19–22]. There are several types of memristive devices whose operation mechanisms are strongly linked to their geometry, and the dielectric and electrode materials employed in their fabrication [4–7,23,24]. For instance, Phase Change Memories [25], which are based on the behavior of phase change materials that can be switched reversibly between amorphous and crystalline phases of different electrical resistivity; Magnetic RAMs [26], that use magnetic and electrical properties exhibited by some materials in particular structures; Ferroelectric devices [27], whose properties are linked to materials with switchable electrical polarization that produce hysteresis curves of the polarization versus electrical field and can be engineered for storing information; finally, the devices with more versatility, Resistive Random Access Memories (RRAMs), where the conduction is linked to internal ion movement and concurrent redox reactions in the dielectric and dielectric/electrode interfaces, which can be used to generate different resistive states in a digital and analog

perspective [28–30]. This manuscript will concentrate on the latter group of devices, RRAMs (also known as resistive memories); in particular, in the extraction procedures that allow obtaining parameters to characterize the resistive switching (RS) operation and the models used to describe the charge conduction features.

Resistive memories have shown outstanding endurance [31] behavior, good retention and low power operation. These devices present a compact crossbar structure ($4F^2$ footprint, where "F" is the minimum technology half-pitch) that is compatible with CMOS technology and low power operation [5]. These devices are being employed as non-volatile memories in commercial fabrication processes. For instance, in the 22 nm node, the following companies incorporate RRAMs: TSMC [32] and INTEL [33]. For this work, we will take into consideration two different types of redox-based devices: electro-chemical metallization cells [23] (also known as conductive bridge RAMs, CBRAMs) and valence change memories (VCMs) [29,34].

We will present here general extraction methodologies for resistive switching parameters. These techniques could work better in one type of device than in others, depending on the operation features and the corresponding current-voltage (I-V) curve shapes that can be obtained both in the quasi-static and transient regimes. In this respect, we account

---

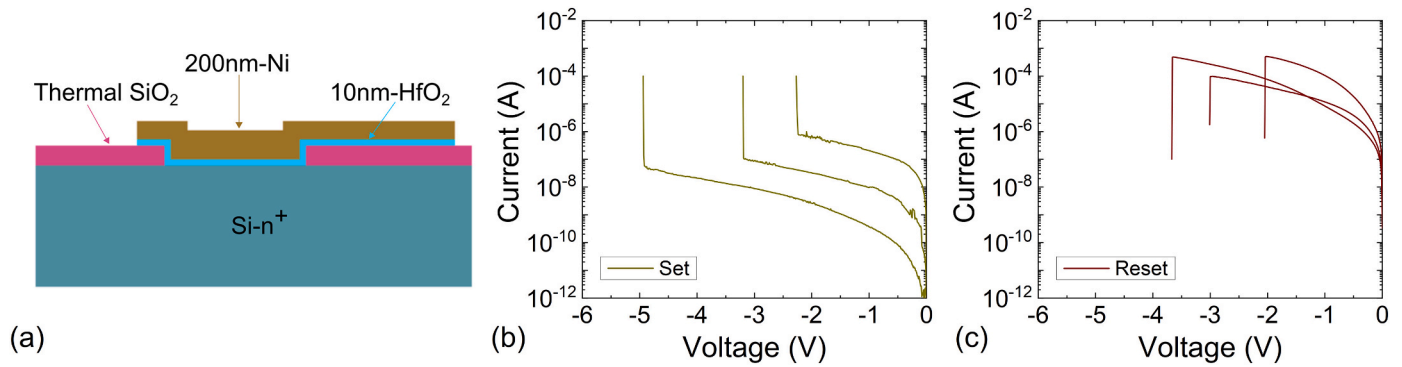**Fig. 1.** a) Schematic cross-section of the unipolar devices based on the Ni/HfO$_2$/Si-n$^+$ stack, b) experimental current versus voltage for the set curves, c) experimental current versus voltage for the reset curves. To prevent permanent dielectric breakdown, a current compliance of 100 µA was employed.

for the fact that there is a wide variety of RRAMs, as different electrodes and dielectrics can be used. Transition metal oxides [35–40] are usually employed, although 2D materials such as graphene oxide [41] or h-BN [21] can also be incorporated. These material associations could lead to filamentary conduction where RS is linked to the formation and rupture of conductive filaments. That is, the set and reset processes that lead to the low resistance state (LRS) and the high resistance state (HRS) are associated to the formation and destruction of CFs that short the electrodes leading to a localized ohmic conduction regime. Other devices show area-dependent conduction that could be attributed to the following conduction mechanisms [29]: Schottky barrier limited transport, where the conduction limiting contact is found at the electronically active electrode; Space Charge Limited Current with a non-exponential voltage dependence that is sometimes employed to explain valence change memories (VCM) cells transport; or Poole-Frenkel conduction where a current process based on trapped charges takes place and the electrons are transported over the dielectric conduction band to the electrode, etc.

Compact models for resistive memories are needed for IC developments. In this field there are open issues such as a good modeling of device-to-device and cycle-to-cycle variability [42–50], thermal effects [51–57], and models accounting for second-order memristors [51,58], even third-order ones [59], etc. Electronic design automation (EDA) tools need the implementation of these compact models for circuit simulation. In addition to the model development efforts, the parameters of these models for each technology have to be determined; in this respect, parameter extraction methodologies are needed. At this point we contextualize this review in which we bring most of the different techniques developed for the extraction of some parameters in resistive memories under one roof [2,60–64]. In this context, the particularities of the experimental current data that cover several orders of magnitude

in the transition from the HRS to LRS and the other way around, the limitations of the measurement equipment, device noise, etc., have to be dealt with the appropriate mathematical techniques [23,48,50,60,63,65–67]. Revision works on parameter extraction techniques for other types of devices (e.g. FET devices) can be found in the literature [68–70]; nevertheless, as far as we know, this has not been done yet for resistive memories.

We will also show detailed device simulations to shed light on the RS operation and assess the appropriateness of the proposed numerical techniques for parameter extraction. We will make use of kinetic Monte Carlo (kMC) simulations [44,47,53,71–74] both for the unipolar [71,75] and bipolar [53,76] devices under consideration in this work; although, other types of simulators [37,56] could also be used.

2. Device fabrication and measurement set-up

The electrochemical metallization (ECM) cells employed in our study are based on the unipolar Ni/HfO$_2$/Si stack. They were fabricated on (100) n-type CZ silicon wafers with resistivity (0.007–0.013) Ω cm. The hafnium oxide layers were 10 nm thick and were grown by atomic layer deposition at 200°C using tetrakis (Dimethylamido)-hafnium (TDMAH) and H$_2$O as precursors, and N$_2$ as carrier and purge gas. More details are available in Ref. [77]. A schematic cross-section of the final device structure is shown in Fig. 1a. The current-voltage curves were measured under ramped voltage stress (RVS) using a HP-4155B semiconductor parameter analyser (SPA). The voltage signal was applied to the top Ni electrode, the Si substrate was grounded. The SPA was connected to the computer via GPIB and controlled using MATLAB. 300 I-V curves were obtained in a RS series with consecutive set and reset cycles after a forming process with a compliance current (I$_{CC}$) of 0.1 mA. Some of the set and reset curves are shown in Fig. 1b and c.
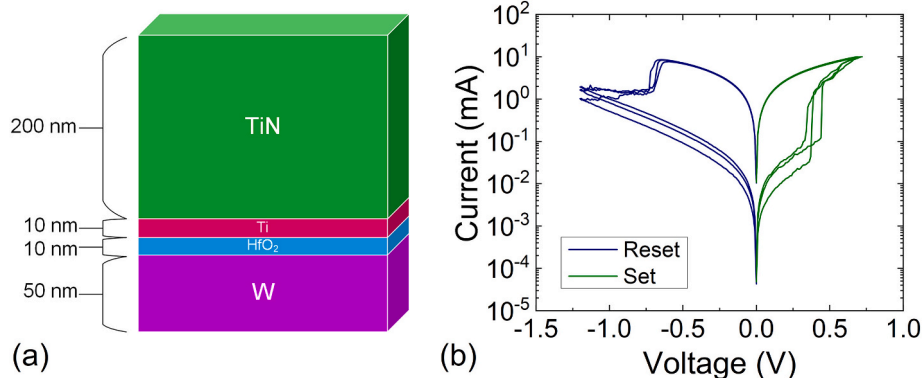
Fig. 2. a) Diagram of the bipolar devices based on the TiN/Ti/HfO$_2$/W stack, b) experimental current versus voltage for some set and reset curves. To prevent the permanent dielectric breakdown, a current compliance of 10 mA was used.
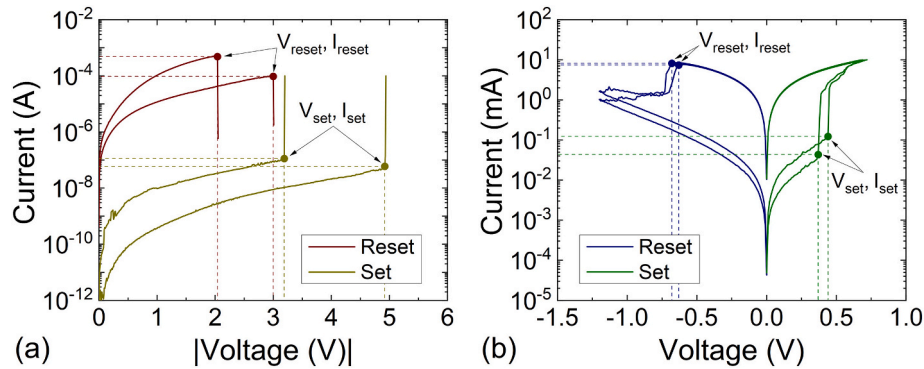
Fig. 3. Experimental current versus voltage curves for a) Ni/HfO$_2$/Si-n$^+$ unipolar and b) TiN/Ti/HfO$_2$/W bipolar devices indicating the set and reset voltages and currents points.

The bipolar VCM devices were built using the TiN/Ti/HfO$_2$/W stack [34]. They were fabricated on a highly-doped N-type ($\rho = 4$ mΩ·cm) silicon wafer. The top metal electrode is a (200 nm TiN/10 nm Ti) bilayer, and the 50 nm-thick W bottom electrode was deposited on a 20 nm-thick Ti adherence layer on the silicon substrate. The 10 nm-thick HfO$_2$ dielectric layer was grown by ALD, see the device layer structure in Fig. 2a. For electrically contacting the W bottom electrode through the highly-doped N-type Si substrate, a 500 nm Al layer was deposited on the back of the wafer by magnetron sputtering. More details are given in Ref. [78]. The I$_{CC}$ was fixed to 10 mA. Again, 300 I-V curves were measured under RVS (Fig. 2b). The RS cycles were programmed with a Matlab software tool that controls a Keysight B1500A SPA via GPIB.

3. Set and reset voltage extraction methods

In this section, we focus on the extraction procedures to obtain the set and reset voltages. These parameters are essential to characterize the transition from the HRS to LRS and the other way around (see Fig. 3). Most papers devoted to experimental RRAMs extract these parameters, although many of them do not clearly state the methodology to do so. As it will be shown below, the numerical technique used for the extraction is linked to the obtained device variability; because of that, the methodological description should be always given.

The great variety of technologies employed for RRAM fabrication produces different I-V curve shapes; some devices can even show unipolar behavior both at positive and negative voltages. Consequently, not all the methodologies presented here fit well for all the different technologies, although they can be adapted in most cases. We will discuss it throughout the manuscript. These extraction techniques work correctly for the devices under consideration here.

See in Fig. 3 that once the set or reset voltages are obtained, the corresponding currents at those values are assumed to be the set and reset currents. From the modeling viewpoint, the set and reset voltages can be useful in behavioral models, where functions such as the hysteron are employed to model the hysteresis loops which could describe well the transitions from LRS to HRS and vice versa, that are inherent to the RS operation [79].

We will consider here I-V curves obtained under ramped voltage stress, the usual characterization procedure for RS operation. The extraction techniques are, therefore, used for these RVS data; however, they could also work well for pulse voltage stress (PVS) operation with none or slight modifications.

3.1. Set voltage extraction

The set process drives the device from the HRS to the LRS. If the conduction is filamentary, one or several CFs are formed that bridge the electrodes. Some of the extraction procedures for the set voltage are given below and they are applied to the two different technologies
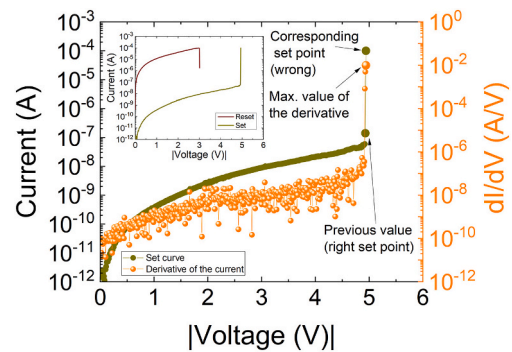

Fig. 4. Experimental current versus voltage curve for a set process corresponding to Ni/HfO$_2$/Si-n$^+$ devices (green circles). The value of the current derivative has been calculated (orange circles) along the curve to extract the set point by detecting the maximum derivative value. See in the inset a complete I-V cycle (set and reset) to clarify which part of the curve is being analyzed. By employing this methodology, the set point might be found in the last point of the curve, leading to an incorrect determination of the set current (the I$_{CC}$). Thus, we have determined the set voltage as the previous value to the calculated one. (For interpretation of the references to colour in this figure legend, the reader is referred to the web version of this article.)
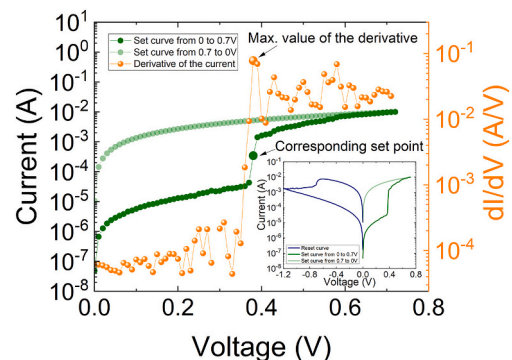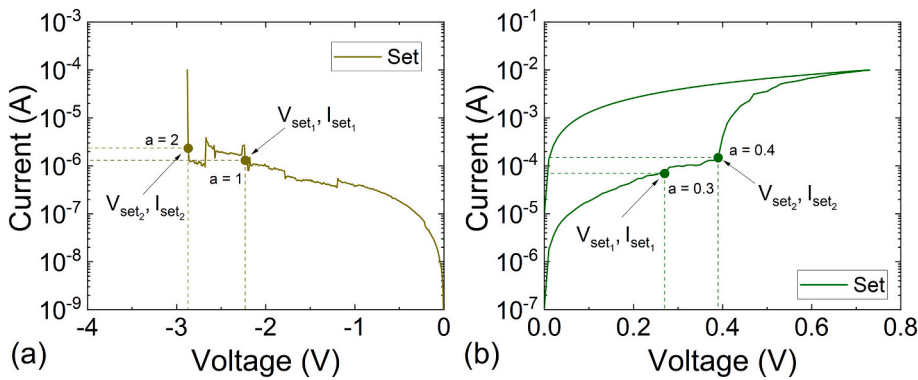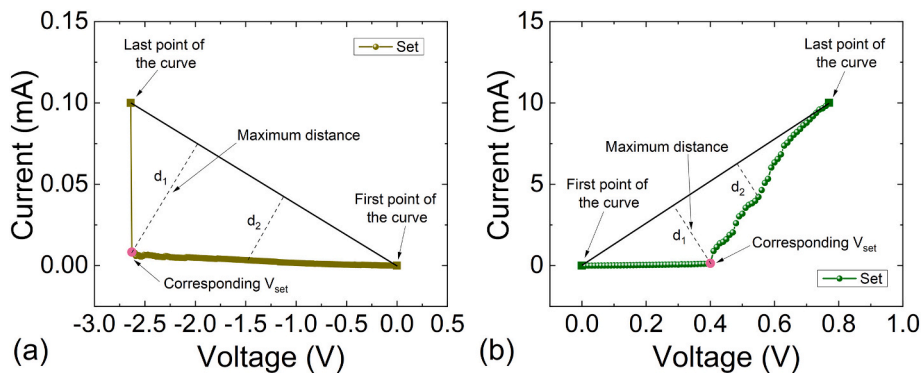

Fig. 5. Experimental current versus voltage curve for a set process corresponding to a TiN/Ti/HfO$_2$/W device (green circles). The value of the derivative has been calculated (orange circles) in the first part of the I-V curve (dark green); i.e., from 0 to 0.7 V to determine the set point, by detecting the maximum derivative value. The inset shows a complete I-V cycle including both set and reset processes, to clarify which part of the curve is being analyzed. (For interpretation of the references to colour in this figure legend, the reader is referred to the web version of this article.)

Fig. 6. Experimental current versus voltage curve for a set process corresponding to a) Ni/HfO$_2$/Si-n$^+$ and b) TiN/Ti/HfO$_2$/W devices. The set point has been established by detecting a current increase in two consecutive points that satisfy the condition I$_{i+1}$ ≥ (1 + a)I$_i$. For the sake of clarity, two parameter values for each curve have been taken into consideration to show the different set voltages obtained. For the unipolar case, shown in a), the a parameter equals 1 and 2, and for the VCM case, shown in b), the a parameters chosen were 0.3 and 0.4.

Fig. 7. Experimental current versus voltage curve for a set process corresponding to a) Ni/HfO$_2$/Si-n$^+$ and b) TiN/Ti/HfO$_2$/W devices. The set point has been established by determining the maximum distance from a straight line that joins the first and last points of the experimental curve.

employed here, i.e., for the ECM and VCM devices described in Section 2.

3.1.1. Maximum current derivative determination (MS1)

The MS1 method is based on the current derivative determination by employing a five-point numerical technique, see Fig. 4 for an example in the unipolar devices under consideration.

This methodology is particularly appropriate for I-V curves with a sudden current rise at the set point, as it is the case for our ECM devices. However, in some curves this technique could lead to the last point of the curve if it is limited by I$_{CC}$. In this case we could have to choose the point prior to the one corresponding to I$_{CC}$ or the antepenultimate. Other technologies give rise to more complex set curves, such as in the bipolar devices case (Fig. 5). The current derivative is also useful to obtain the set voltage in this case, although the extraction is not that clear. That is why we limit the voltage range where the methodology is applied (in our

case located in the [0, 0.7 V] interval), in order to avoid the onward region where random curve shape modifications could generate derivative values leading to an erroneous extraction [80].

3.1.2. Current increase in two consecutive points (MS2)

Another conventional methodology employed consist in detecting a certain current increase in two consecutive points (V$_{set}$ = V$_i$ if I$_{i+1}$ ≥ (1 + a)I$_i$) [56].

We employed a = 1 and a = 2 for the unipolar devices (Fig. 6a). Note that higher a parameter values work better assuming the sudden current rise that takes place at the set point. An a = 1 value could lead to error in some curves (V$_{set1}$ in Fig. 6a) if a non-fully realized set processes is found; however, for higher values, a ≥ 1.5 the real set voltage (V$_{set2}$ in Fig. 6a) can be detected. If the a parameter value is too high, it will lead to an undetected set voltage, therefore, a tuning process is necessary for each technology.
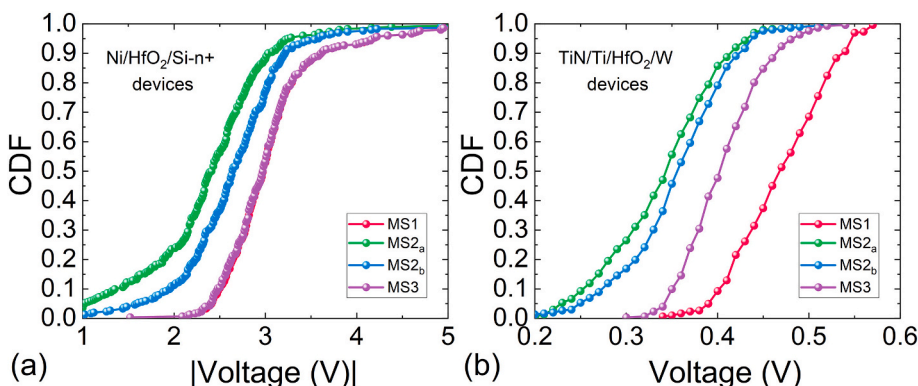
Fig. 8. Cumulative distribution functions for the 300 set processes measured in (a) Ni/HfO$_2$/Si-n$^+$, (b) TiN/Ti/HfO$_2$/W devices comparing the extraction methods discussed above. MS1 corresponds to the maximum current derivative value, MS2$_a$ to a current increase in two consecutive points assuming a = 1, MS2$_b$ to a current increase in two consecutive points assuming a = 2 for (a); and a = 0.3 for MS2$_a$ and a = 0.4 for MS2$_b$ for (b), and MS3 to the maximum separation from a straight line from the experimental curve. In the a) panel MR1 and MR3 almost overlap.

Table 1

Mean, standard deviation and coefficient of variation (ratio of the standard deviation to the mean) for the devices under study in the set case. All the methods discussed above have been considered.

Method	Ni/HfO$_2$/Si-n$^+$ devices				TiN/Ti/HfO$_2$/W devices			
	MS1	MS2$_a$	MS2$_b$	MS3	MS1	MS2$_a$	MS2$_b$	MS3
Mean, μ (V)	3.05	2.36	2.64	3.04	0.47	0.34	0.36	0.41
Standard deviation, σ (V)	0.56	0.67	0.61	0.56	0.05	0.06	0.07	0.04
Coefficient of variation	0.18	0.28	0.23	0.18	0.11	0.19	0.18	0.10

For the bipolar devices, commonly, a parameter values in the [0.3, 0.4] interval work well. Nevertheless, the results for a = 0.3 are not correct (V$_{set1}$ in Fig. 6b). But for a ≥ 0.4 good results are obtained (V$_{set2}$ in Fig. 6b). Therefore, a fitting process is needed for the whole data set obtained in the RS series, since the a parameters are constant for the whole RS series. This methodology also works for technologies different from the ones evaluated here as shown in Ref. [56]. Finally, we call the reader's attention to the fact that the a parameter choice could be connected with the voltage step employed in the measurements and the applied voltage ramp rate. This issue has to be considered in the a parameter fitting process.

3.1.3. Maximum separation from a straight line that joins the first and end points in a set curve (MS3)

The technique MS3 was developed in Ref. [80]. It is based on finding the maximum separation of the measured curve to an imaginary straight line that joins the first point measured at null voltage and the first point when the compliance current is reached (Fig. 7). Our main pursue here is the determination of the set curve knee (see Fig. 7). The experimental curve is shown from the beginning of the measurement (V$_{Applied}$ = 0 V) till the end of the voltage ramp. Then, the greatest distance, d$_{max}$, between the experimental curve and the straight line determines the set voltage V$_{set}$ (Fig. 7).

The whole set of results of the techniques described above are shown in Fig. 8 for the two technologies we are considering. The cumulative distribution functions (CDF) are plotted versus voltage, this is a common manner to evaluate cycle-to-cycle variability. It can be seen that the measured C2C variability depends on the extraction technique, as shown in [80].

The lower variability corresponds to the MS3 technique. The calculation of the coefficient of variation (CV, ratio of the standard deviation to mean) allows a quantitative description of variability, see Table 1. In the bipolar devices, a slightly higher variability is obtained in the MS1 with respect to MS3, this latter result could be connected to the variations linked to the derivative calculation and the I-V curve shape; nevertheless, in the unipolar case, since the maximum derivative is clearly found at the end of the set point, MS1 and MS3 are similar in terms of the CV and the corresponding CDFs overlap. The higher variability is obtained for the MS2 method, and as it would be expected, it depends on the a parameter. The variations in the formation of the conductive filaments that facilitate resistive switching operation produce current changes along the I-V curve (as the set and reset processes evolve) and these effects could lead to the changes that come out from method MS2 for different a parameters.

3.2. Reset voltage extraction

The reset process increases the device resistance from the LRS to the HRS. In case of filamentary conduction, the CFs that short the electrodes are destroyed, and the dielectric high resistivity is partially recovered. The different numerical techniques for the reset voltage determination can be linked to the stages of CF rupture that the device undergoes in the reset process [56], although this is not an easy task due to the inherent stochasticity of RS operation. Kinetic Monte Carlo simulations can be used to deepen on the RS dynamics as it will be shown below. In addition, advanced statistical techniques, such as these based on phase-type
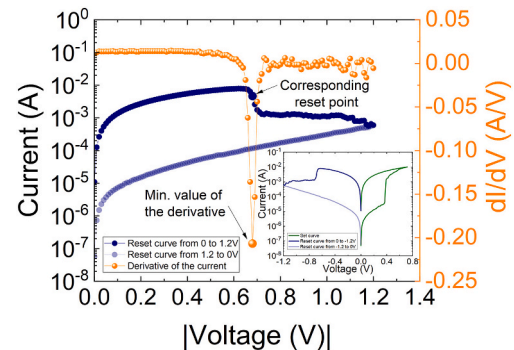

Fig. 9. Experimental current versus voltage curve for a reset process measured in TiN/Ti/HfO$_2$/W devices (blue circles). The value of the derivative has been obtained (orange circles) in the first part of the I-V curve (dark blue); i.e., from 0 to 1.2 V, to determine the reset point by detecting the minimum derivative. The inset shows a complete I-V cycle, including set and reset processes. (For interpretation of the references to colour in this figure legend, the reader is referred to the web version of this article.)

distributions, can be employed to characterize the CF destruction stages along a reset process [62,67,81,82].

The most representative extraction techniques for the reset parameters are described below. As in the previous section, we will employ both the ECM and VCM devices under consideration here.

### 3.2.1. Minimum current derivative determination (MR1)

The technique MR1 uses the current derivative determination by employing a five-point numerical differentiation to extract the reset voltage and current. An example is given in Fig. 9 for the bipolar devices, see that the minimum derivative occurs at the region where the more pronounced current decrease is found, as expected. For this technology, the technique works well even though there are other curve sections where the current drop takes place because of the inherent device stochasticity.

As can be seen in Fig. 1c, the abrupt current drop that takes place in the unipolar devices at the end of the I-V allows an easy determination of the reset voltage using this technique. Even in the case of current jumps along the I-V curve, the higher derivative is clearly found at the end of the curve, corresponding to the CF rupture.

3.2.2. Current decrease in two consecutive points (MR2)

A decrease in two current consecutive points can be used to extract the reset voltage (V$_{reset}$ = V$_i$ if I$_{i+1}$ ≤ (1 + a)I$_i$) [56,80]. As in the case of the set voltage determination, the a parameters that work well depend on the particular RRAM technology.

For both type of devices under consideration here we have employed a = 0.05 and a = 0.1 to assess the different reset voltages extracted. The a = 0.05 case is not good enough to circumvent the usual RS current variations in a I-V curve for the unipolar devices; therefore, a = 0.1 was chosen. See that the expected results are then reached in this latter case (Fig. 10a). A trade-off is needed for each technology since a very high a parameter could prevent the obtention of any reset voltage along the I-V curve. As highlighted above, the measurement features such as the
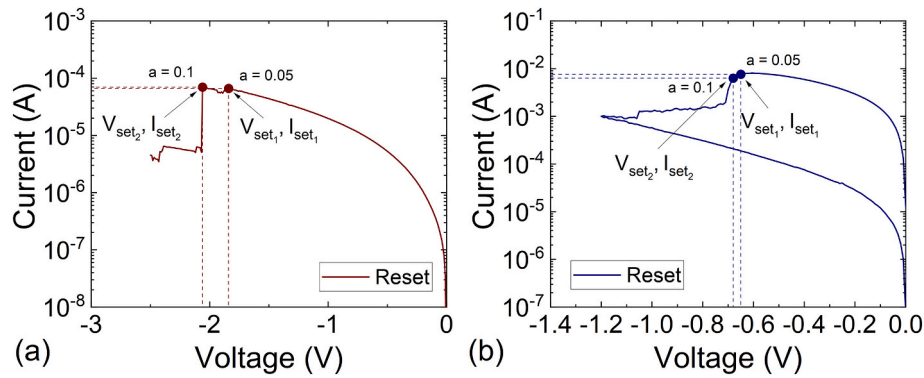
Fig. 10. Experimental current versus voltage curve for a reset process measured in a) Ni/HfO$_2$/Si-n$^+$, b) TiN/Ti/HfO$_2$/W devices. The reset point has been established by detecting a current decrease in two consecutive points that satisfies the condition I$_{i+1}$ ≤ (1 + a)I$_i$. Two a values for each curve have been employed to show the different reset voltages obtained (a equals 0.05 and 0.1 for both unipolar and bipolar devices).
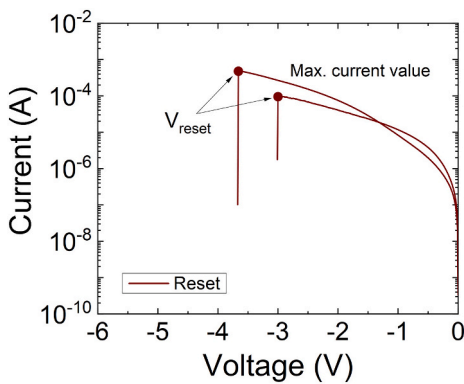
Fig. 11. Experimental current versus voltage curves for two reset processes measured in Ni/HfO$_2$/Si-n$^+$ devices. The reset point in MR3 is established by assuming the maximum value of the current in all the curves.
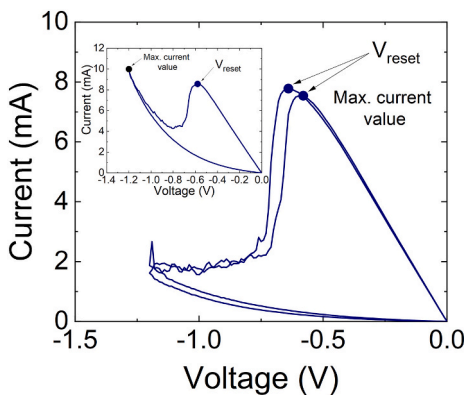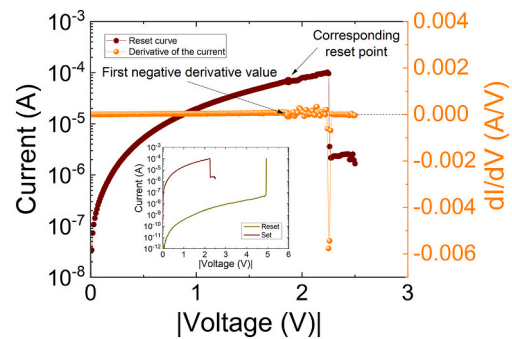

Fig. 12. Experimental current versus voltage curves for two reset processes measured in TiN/Ti/HfO$_2$/W devices. The reset point in MR3 is established by assuming the maximum value of the current in all the voltage interval considered.

voltage step and the applied voltage ramp rate have to be taken into account since the election of the a parameter could be linked to them.

3.2.3. Determination of the current maximum (MR3)

This methodology has been employed previously in Refs. [80, 83]. It is an interesting technique since no indeterminations are produced in most cases. It works well for many technologies, including the two we are assuming here, see Figs. 11 and 12.


Fig. 13. Experimental current versus voltage for a reset process measured in a Ni/HfO$_2$/Si-n + device (brown colour circles). The value of the derivative (calculated with the simplest two-point formulae) has been calculated (orange circles) along the I-V curve to obtain the reset point by detecting the first negative value of the derivative. A complete I-V cycle is plotted in the inset to clarify which part of the curve is employed. (For interpretation of the references to colour in this figure legend, the reader is referred to the web version of this article.)
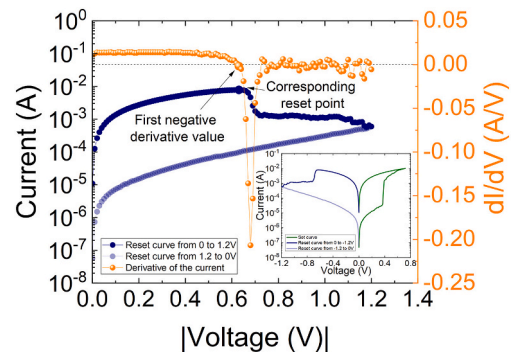
Fig. 14. Experimental current versus voltage curve for a reset process measured in a TiN/Ti/HfO$_2$/W device (blue circles). The value of the derivative has been calculated (orange circles) in the first part of the I-V curve (dark blue) to obtain the reset point by detecting the first negative value of the derivative. (For interpretation of the references to colour in this figure legend, the reader is referred to the web version of this article.)

Although the current drop in the bipolar devices is not as abrupt as in the unipolar case, this MR3 technique works well. Note that, as shown in the inset in Fig. 12, this method could lead us to detect wrong reset voltages at high voltages. Because of this, for this VCM technology, the interval to check this condition is limited from 30% to 80% of the
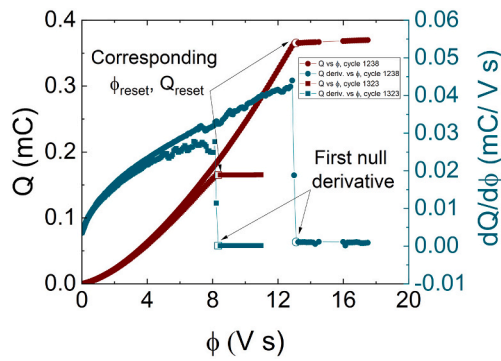
Fig. 15. Calculated charge versus flux curve for two reset processes measured in a Ni/HfO$_2$/Si-n$^+$ device (brown symbols). The value of the derivative for the charge has been calculated (dark cyan) along the I-V curve to obtain the reset point by detecting the first zero derivative value. (For interpretation of the references to colour in this figure legend, the reader is referred to the web version of this article.)

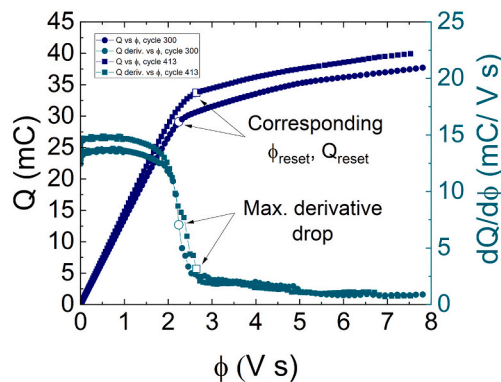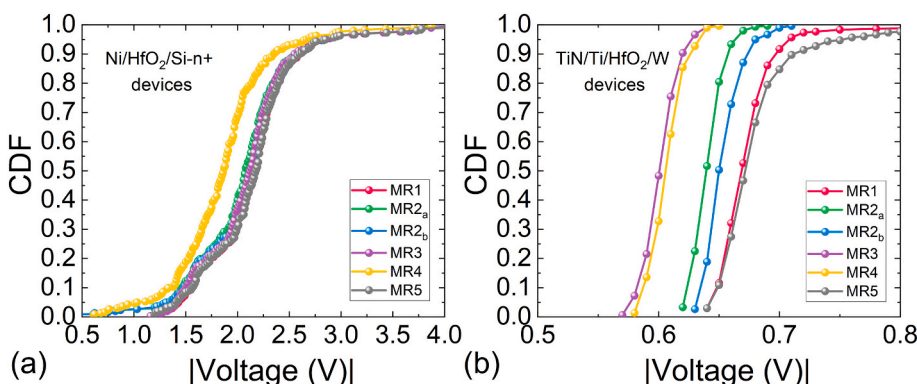**Fig. 16.** Calculated charge versus flux curve for two reset processes measured in TiN/Ti/HfO$_2$/W devices (blue symbols). The value of the derivative has been calculated (dark cyan symbols) to obtain the reset point by detecting the maximum derivative drop. (For interpretation of the references to colour in this figure legend, the reader is referred to the web version of this article.)

voltage variation range.

3.2.4. First point with decreasing current (MR4)

This technique was proposed in [56]. It allows to build a robust algorithm, although it is much more sensitive to RS current jumps than the previous ones. In here (Fig. 13) a simple two-points formula is employed for the derivative calculation since we are just interested in the first negative derivative value.

The use of this technique in our bipolar devices produces also different results from MR1, as can be seen in Fig. 14.

3.2.5. Null charge derivative in the charge-flux domain (MR5)

If we represent the experimental I-V curves in the charge-flux domain [2,65,84] (see the Appendix), a simple representation is obtained (Fig. 15). If we perform the charge derivative with respect to the flux and detect when this derivative is null, a new methodology for the reset voltage determination comes up by means of determining the (Q_{reset}, ϕ_{reset}) values [61].

This method must be modified for bipolar devices since the Q-ϕ curves are different from those obtained for ECM devices. For bipolar devices (Fig. 16) there is no saturation of the Q value, and correspondingly no null Q-ϕ derivatives; in this respect, we use the maximum charge derivative decrease along the curve to obtain the (Q_{reset}, ϕ_{reset}) pairs that allow the calculate the reset voltage.

Taking into consideration all the methodologies described above for the reset voltage extraction, we were able to obtain the CDFs, see Fig. 17.

For the ECM technology, all the methodologies produce similar outputs save MR4, which is affected by the RS variations when determining the first point with decreasing current. Due to the I-V curve shape in the VCM case, the different techniques produce separated CDF curves, although in terms of the CV (Table 2), i.e. the variability estimated, the results are similar for MR2, MR3 and MR4. It is clear that VCM devices show a much lower variability; in this respect, they would better work for non-volatile memory applications.

As pointed out above, the fitting parameters and subtleties of the numerical implementation have to be adapted to each particular technology. The set and reset voltage variability depends on the numerical extraction procedure for each type of device. In this respect, when analyzing the C2C variability, the numerical technique employed to extract the RS parameters should be explained. In addition to the methods described above, others could be employed, such as using a determined current threshold (or a resistance threshold) to extract the set and reset voltages [83,85].

3.3. Kinetic Monte Carlo analysis

We have included kMC simulations to complement the study and explore the goodness of the techniques proposed here. To do so, kMC tools developed for the technologies used here were employed, see [53,71]. The CF rupture process in the reset curve of the ECM devices (black in Fig. 18A) takes place in the curve section where the current drops off (see the c) to d) CF snapshots in Fig. 18, the percolation path is broken in d)). A similar consideration can be pointed out for the set process, but at the percolation path level, it is the other way around. In this respect, all the numerical methods suggested here are coherent with the detailed kMC simulation since they extract the reset (set) voltage at the sudden and great current drop (rise) at the end of the I-V curve.

Fig. 17. Cumulative distribution functions for the 300 reset processes measured in a) Ni/HfO$_2$/Si-n$^+$, b) TiN/Ti/HfO$_2$/W devices comparing the extraction methods discussed above. MR1 corresponds to the minimum current derivative value, MR2$_a$ (MR2$_b$) to a current decrease in two consecutive points assuming a = 0.05 (a = 0.1), MR3 to the maximum current along the reset curve, MR4 to the first negative value of the derivative and MR5 to extract the reset voltage at the point of null charge derivative (a) and maximum decrease in the charge derivative (b) in the charge-flux domain.

Table 2
Mean, standard deviation and coefficient of variation (ratio of the standard deviation to the mean) for the devices under study in the reset case. All the methods discussed above have been considered.

| Method	Ni/HfO$_2$/Si-n$^+$ devices						TiN/Ti/HfO$_2$/W devices					
	MR1	MR2$_a$	MR2$_b$	MR3	MR4	MR5	MR1	MR2$_a$	MR2$_b$	MR3	MR4	MR5
Mean, μ (V)	2.14	2.07	2.09	2.11	1.86	2.15	0.68	0.64	0.66	0.61	0.61	0.68
Standard deviation, σ (V)	0.47	0.51	0.52	0.46	0.48	0.47	0.03	0.01	0.02	0.01	0.01	0.03
Coefficient of variation	0.22	0.24	0.25	0.22	0.26	0.22	0.04	0.02	0.02	0.02	0.02	0.05
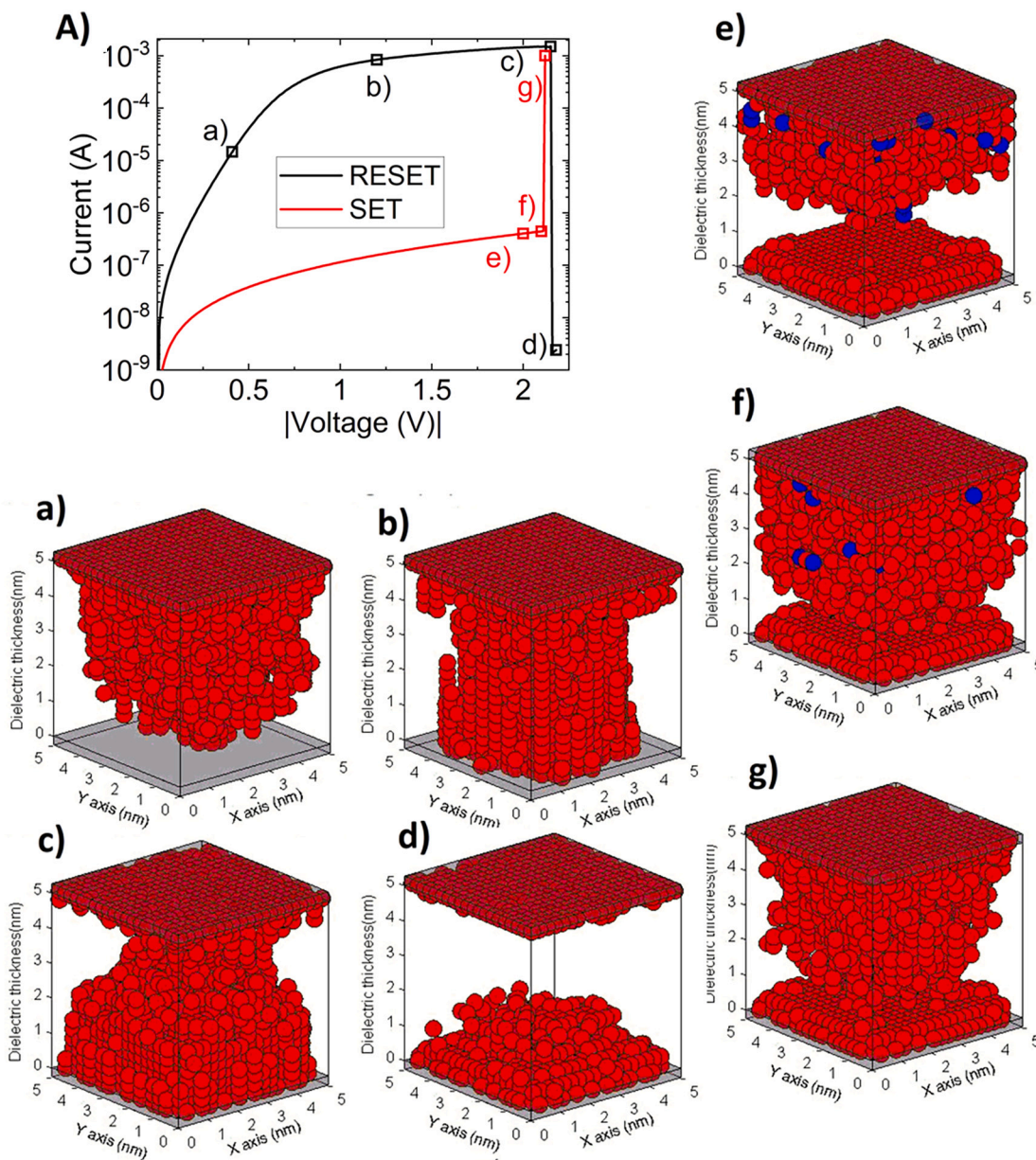
Fig. 18. A) Current versus voltage curves obtained using the kMC technique [71], which includes the 3D description of the electric field and temperature distributions. It shows typical I-V curves for the reset (black) and set (red) processes for the unipolar Conductive Bridge RAMs based on Ni/HfO$_2$/Si-n$^+$ devices here. The reset and set curves are labeled (a–g) at different stages of the CF evolution to illustrate the RS operation and the onset of reset and set events. In the conductive filament figures, corresponding to the device dielectric, red balls represent Ni atoms and the blue ones represent Ni cations. When the Ni atoms form a complete CF (i. e., a percolation path is fully formed), the simulation only shows Ni atoms (reduced atoms) within the simulation domain. (For interpretation of the references to colour in this figure legend, the reader is referred to the web version of this article.)

For the bipolar devices (Fig. 19 for the kMC analysis), the formation and rupture events are not so obvious, both experimentally and in kMC simulation, see [53]. In the reset curve, at negative voltages, the CF is broken in c) (where the oxygen ions are shown in the CF snapshot). At this point the CF temperature is lower in comparison to points a) and b), as it should be since the dissipated power is lower (the average CF temperature is shown in Fig. 19B, notice that it is much lower than at the CF hottest point corresponding to the CF narrowing where the current
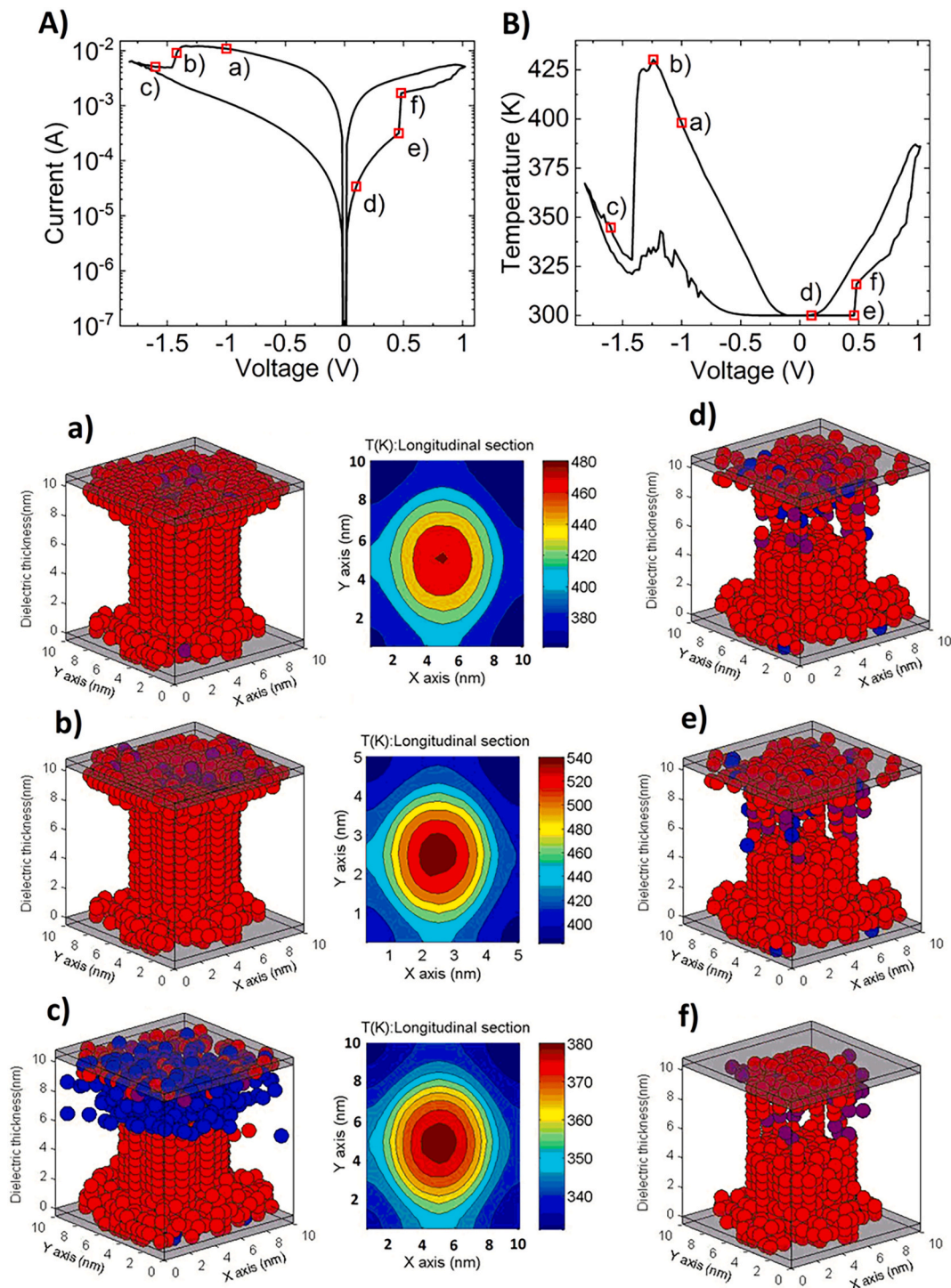
Fig. 19. The I-V curves and conductive filament snapshots are simulated using a kMC-based simulator for the VCM devices based on TiN/Ti/HfO₂/W stacks [53]. In addition to the kMC algorithm, the 3D electric field and temperature distributions are obtained in the simulation domain. A) It shows a typical I-V cycle (set and reset). B) It shows the mean CF temperature along the resistive switching cycle represented in A). The labels correspond to the same conductive filament stages marked in A). These CF stages are taken along the reset and set curves. For some of these stages (points in the reset curve) the temperature contour maps are given (XY cross-sections in the middle of the dielectric). See that the conductive filaments present irregularities and holes, that is why the temperature contour lines are not symmetrical. In the conductive filament plots, the red balls stand for oxygen vacancies, the blue balls for oxygen ions and the purple ones are both an oxygen vacancy and an oxygen ion in the same grid point (not recombined yet). Oxygen ions are plotted only when the percolation path is broken. (For interpretation of the references to colour in this figure legend, the reader is referred to the web version of this article.)

lines concentrate). In b) the CF is close to rupture, in fact, as shown in [80] in another kMC simulation, the CF could be broken at the end of the current drop section; however, in this case, it takes a higher voltage to reset. The device inherent stochasticity makes the CFs get ruptured at different points along the reset curve in different cycles. However, it seems that the percolation paths are broken once the maximum current point is left behind in the reset curve; therefore, other methodologies (different to MR3) could be considered more physically based according
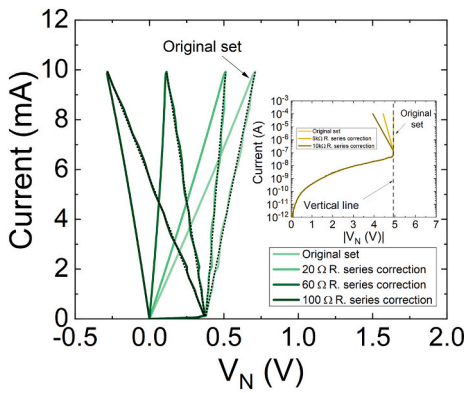
Fig. 20. Experimental current versus modified voltage (V_N) for a set process measured in a TiN/Ti/HfO$_2$/W device. To obtain these plots, a series resistance correction has been performed assuming $V_N = V_{measured} - I_{Measured} \times R_{series}$ and successively sweeping the value of R_{series}. Black dotted lines mark the linear regression obtained in the part of the curve accounting with the highest slope. See in the inset an experimental current versus modified voltage for a set process measured in a Ni/HfO$_2$/Si-n$^+$ device. As can be seen, the presented methodology does not work well for this unipolar technology.
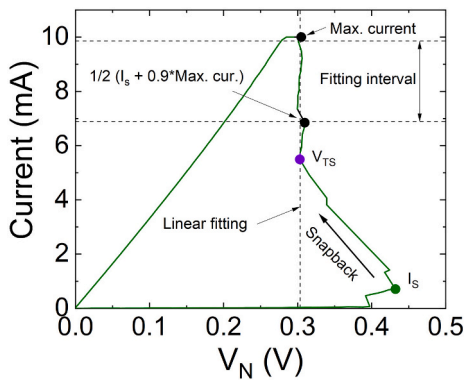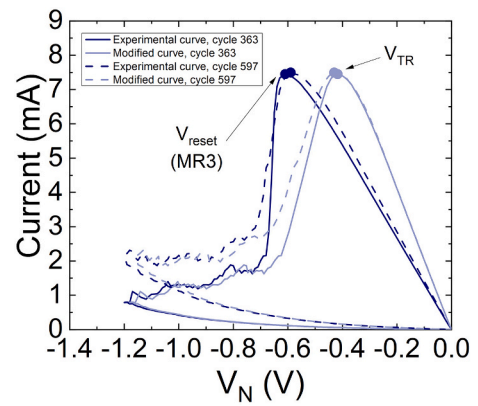

Fig. 21. Experimental set current versus modified voltage (V_N) for a TiN/Ti/HfO$_2$/W device. A series resistance correction = 39.5 Ω has been selected assuming $V_N = V_{measured} - I_{Measured} \times R_{series}$. The fitting interval is indicated with two dashed horizontal lines comprising between 0.9*(current maximum) and ½* (I_s + 0.9*(current maximum)). The black dashed vertical line marks the linear regression obtained in the part of the curve accounting with the highest slope.

to the correspondence to kMC simulations, such as MR1, MR2. MR4 is closer to kMC results than MR3; MR1 and MR2 fit better than MR4 to kMC since they provide reset voltages higher than MR3 and MR4. In relation to MR5, although their reset voltages are found closer to those from MR1 and MR2 methods, its links to the kMC results are weaker since the charge and flux magnitudes employed in MR5 are more complex (see the appendix). Temperature cross-sections in the middle of the dielectric are given for the CF snapshots a)–c). They show reasonable results: the temperature rise as the reset process goes on till the CF is ruptured, where a sudden cool down process takes place. The temperature contour plots change both quantitatively and in shape due to the CF evolution.

4. Series resistance determination

The series resistance is an important parameter to consider when analyzing and modeling resistive memories [86–89]. This parameter can be employed to improve compact models such as the Stanford model [52,64,90–92] to better fit experimental I-V curves measured under RVS and analyze RS operation.


Fig. 22. Experimental current versus modified voltage (V_N) for two reset processes in a TiN/Ti/HfO$_2$/W device. A series resistance correction of 25.8 Ω and 21.3 Ω for cycles 363 and 597 respectively has been selected. V_{reset} is calculated by using MR3 (maximum current value) while the reset transition voltage, V_{TR}, is calculated in the same manner in the modified curve ($I_{measured}$, V_N).
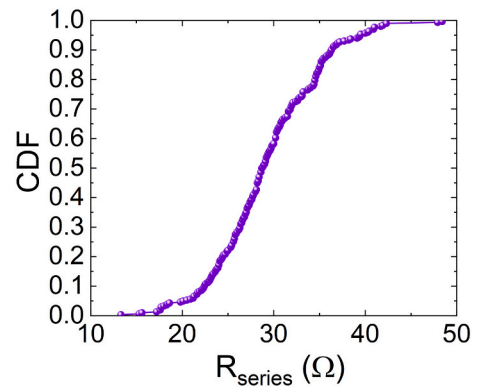
Fig. 23. Cumulative distribution function for the series resistances extracted in TiN/Ti/HfO$_2$/W devices employing the methodology described above.

The extraction method makes use of a newly defined voltage $V_N = V_{Applied} - I_{Measured} \times R_{series}$; $V_{Applied}$ is the device external applied voltage and $I_{Measured}$ stands for the measured current. If the experimental current is plotted versus V_N, sweeping R_{series}, we get modified $I_{Measured} - V_N$ curves (Fig. 20).

We chose in our methodology the curve with the steepest slope in the region after the curve knee. As highlighted in [63,64,89], a vertical curve behavior suggests a sustained conductive filament growth that
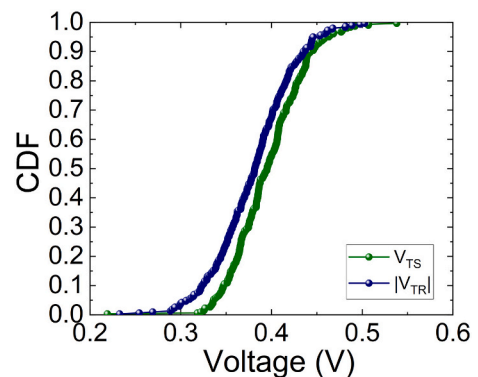
Fig. 24. Cumulative distributions functions for the transition voltages V_{TS} and V_{TR} in TiN/Ti/HfO$_2$/W devices. Note that the values obtained are very similar as expected.
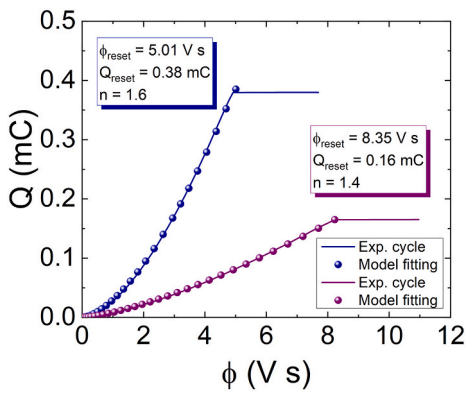
Fig. 25. Calculated charge versus flux curve for two reset processes measured in Ni/HfO$_2$/Si-n$^+$ devices (solid lines). Taking into consideration Eq. A3, these charge-flux curves have been fitted by assuming $n = 1.6$ and $n = 1.4$ respectively (shown in symbols).

leads to a current rise even if the voltage in the active part of the device is fixed. The slope of the curve is obtained by means of a linear regression scheme where the limits are conveniently taken at 90% of the curve maximum current and the average between the latter value and I_S (obtained at the point where the set voltage is determined in the original experimental curve), as explained in [64].

As highlighted in [80], at the end of the set curve, when the filament can no longer expand, the process slows down, which can be regarded as the appearance of an additional series resistance. The snapback effect can be observed in the curve in Fig. 21 [87–89]. R_{series} is extracted making use of the set curves, then the reset curves can be replotted using V_N, see Fig. 22.

After the series resistance is calculated, the set (V_{TS}) and reset (V_{TR}) transition voltages can be obtained from the modified curves. V_{TR} is obtained with the MR3 methodology in the modified curve, see Fig. 22; while V_{TS} is determined in the vertical section of the modified set curve in Fig. 21.

The series resistance CDF is plotted in Fig. 23 for the 300 cycles analyzed, these values are in the interval of those extracted in [65].

In addition, the V_{TS} and V_{TR} CDFs are given in Fig. 24. The set and reset transition voltages are similar due to the importance of the electric field dependence of the corresponding RS operation.

5. Charge-flux modeling and parameter extraction

We analyze here the parameters introduced in Section 3.2.5, in the context of the charge-flux approach (Q_{reset}, ϕ_{reset} and n). Under the context described in the Appendix, we unfold a semiempirical model that fits the experimental data in a reasonable manner [2,84]. At the

reset point, Q_{reset} and ϕ_{reset} can be determined by detecting the first null value of the charge derivative with respect to the flux, as indicated in Fig. 15 for Ni/HfO$_2$/Si-n$^+$ devices. See the values obtained for some Q-ϕ curves in Fig. 25.

After processing all the measured curves for Ni/HfO$_2$/Si-n$^+$ devices, the cumulative distribution functions for Q_{reset} and ϕ_{reset} were obtained and plotted in Fig. 26.

See that C2C variability could be studied based on these magnitudes instead of the set and reset voltages. In the case of using Q_{reset} and ϕ_{reset}, due to the properties of the integrals employed for the calculations (Eqs. A1 and A2), the effects of measurement noise and RS variations would be reduced.

According to Eq. A3, a full modeling process can be performed of the charge-flux data. The *n* value was determined by minimizing the mean squared error between the modeled and experimental data. We have performed the modeling process for all the RS cycles considered for the ECM devices and the *n* values obtained, found to be in the [1.3, 1.95] interval, are shown in Fig. 27.

The analysis in terms of the charge-flux domain has also been performed for the technology based on the TiN/Ti/HfO$_2$/W stack (Fig. 28).

The fittings performed with Eq. A3 work well with n parameters in the [0.9, 0.95] interval for the VCM devices.

6. Conclusions

A revision of parameter extraction techniques for resistive memories has been presented. Different numerical methodologies have been explained for the extraction of the reset and set voltages and corresponding currents, the series resistance and the parameters needed in a charge-flux modeling approach. These techniques have been applied for
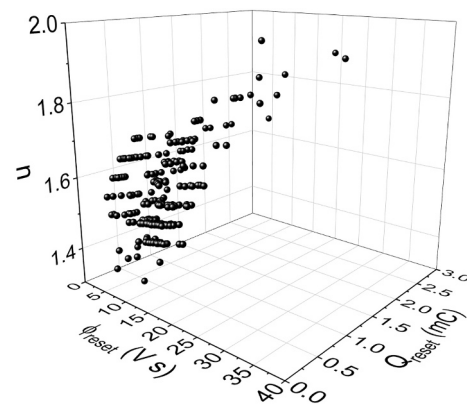
Fig. 27. n parameter versus Q_{reset}, ϕ_{reset} for Ni/HfO$_2$/Si-n$^+$ devices obtained by means of Eq. A3.
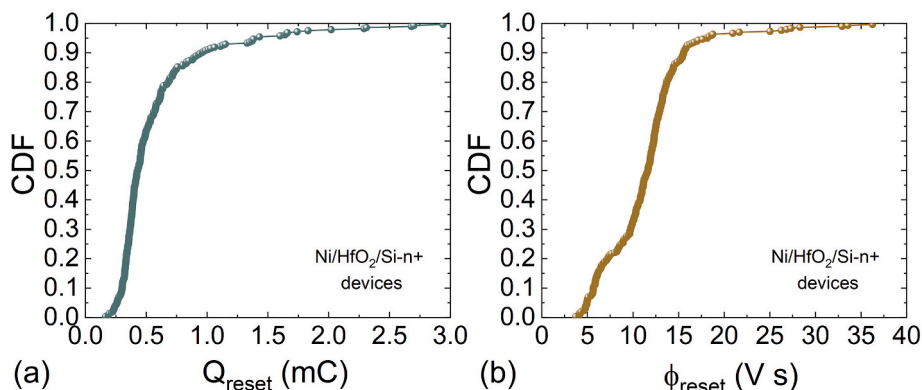
Fig. 26. Cumulative distributions functions for a) Q_{reset}, b) ϕ_{reset} extracted in Ni/HfO$_2$/Si-n$^+$ devices for the 300 cycles analyzed.
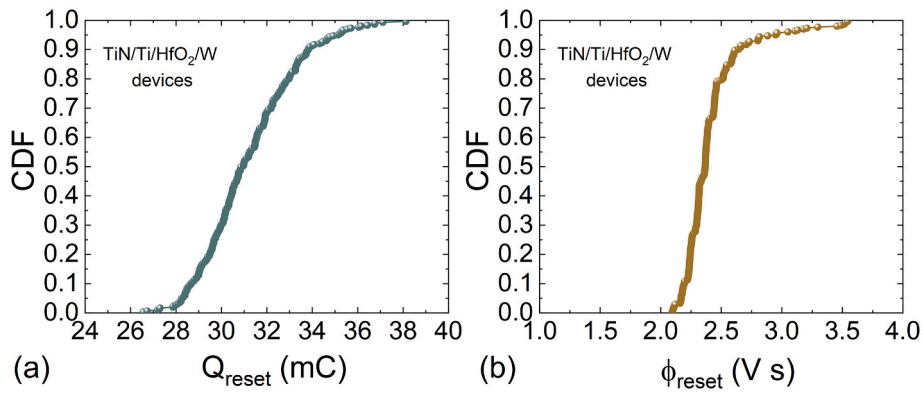
Fig. 28. Cumulative distributions functions for a) Q_{reset}, b) ϕ_{reset} extracted in TiN/Ti/HfO$_2$/W devices for the 300 cycles analyzed.

ECM unipolar and VCM bipolar RRAMs and the numerical issues related have been described in depth. It has been shown that the numerical techniques must be adapted to each technology due to the different I-V curve shapes that are obtained for each device type. The cycle-to-cycle variability of each parameter depends on the methodology employed for their extraction, this is an important result that makes essential the description of the techniques employed to extract the resistive switching parameters in each case. In addition to the discussion of the techniques and their application on wide experimental data sets, kinetic Monte Carlo simulations were used to assess the accuracy of the numerical techniques presented here by analyzing the formation and rupture of the percolation paths that constitute the conductive filaments that allow resistive switching operation.

Declaration of Competing Interest

The authors declare that they have no known competing financial interests or personal relationships that could have appeared to influence the work reported in this paper.

Acknowledgments

Appendix. Charge-flux modeling

For the calculations in the charge-flux domain, characteristic of memristive device modeling [2,84], the charge is obtained from the conventional I-V curves as follows,

$$Q(t) = \int_0^t i(t') \, dt' \tag{A1}$$

where i(t) and v(t) are the measured current and voltage. Eq. A2 depicts the flux calculation,

$$\phi(t) = \int_0^t v(t') \, dt' \tag{A2}$$

We have calculated the integrals by means of the trapezoidal rule.

A model in the charge-flux domain has been employed to fit experimental data for the devices we are considering here [2,84]. See Eq. A3.

$$Q(\phi) = Q_{reset} \left(\frac{\phi}{\phi_{reset}} \right)^n \tag{A3}$$

where Q_{reset} and ϕ_{reset} (Section 3.2.5) are obtained at the reset point and n is a fitting parameter.

References

[1] L.O. Chua, K.S. Mo, Memristive devices and systems, Proc. IEEE 64 (2) (1976) 209–223.

[2] M.M. Al Chawa, R. Picos, J.B. Roldán, F. Jiménez-Molinos, M.A. Villena, C. de Benito, Exploring resistive switching based memristors in the charge-flux domain, a modeling approach, Int. J. Circ. Theory Appl. 46 (2018) 29–38.

[3] Mario Lanza, Abu Sebastian, Wei D. Lu, Manuel Le Gallo, Meng-Fan Chang, Deji Akinwande, Francesco M. Puglisi, Husam N. Alshareef, Ming Liu, Juan B. Roldan, Memristive technologies for data storage, computation, encryption and radio-frequency communication, Science 376 (6597) (2022) 1–13.

[4] M. Lanza, H.-S.P. Wong, E. Pop, D. Ielmini, D. Strukov, B.C. Regan, L. Larcher, M. A. Villena, J.J. Yang, L. Goux, A. Belmonte, Y. Yang, F.M. Puglisi, J. Kang, B. Magyari-Köpe, E. Yalon, A. Kenyon, M. Buckwell, A. Mehonic, A. Shluger, H. Li, T.-H. Hou, B. Hudec, D. Akinwande, R. Ge, S. Ambrogio, J.B. Roldan, E. Miranda, J. Suñe, K.L. Pey, X. Wu, N. Raghavan, E. Wu, W.D. Lu, G. Navarro, W. Zhang, H. Wu, R. Li, A. Holleitner, U. Wurstbauer, M. Lemme, M. Liu, S. Long, Q. Liu, H. Lv, A. Padovani, P. Pavan, I. Valov, X. Jing, T. Han, K. Zhu, S. Chen, F. Hui, Y. Shi, Recommended methods to study resistive switching devices, Adv. Electron. Mater. 5 (2019) 1800143.

[5] S. Spiga, A. Sebastian, D. Querlioz, B. Rajendran, Memristive Devices for Brain-Inspired Computing, Elsevier, 2020.

[6] F. Pan, S. Gao, C. Chen, C. Song, F. Zeng, Recent progress in resistive random-access memories: materials, switching mechanisms and performance, Mater. Sci. Eng. 83 (2014) 1–59.

[7] J.S. Lee, S. Lee, T.W. Noh, Resistive switching phenomena: a review of statistical physics approaches, Appl. Phys. Rev. 2 (2015), 031303.

[8] S. Ambrogio, et al., Equivalent-accuracy accelerated neural-network training using analogue memory, Nature 558 (2018) 60–67.

[9] K. Zhu, M.R. Mahmoodi, Z. Fahimi, Y. Xiao, T. Wang, K. Bukvišová, M. Kolíbal, J. B. Roldan, D. Perez, F. Aguirre, M. Lanza, Memristors with initial low resistive state for efficient neuromorphic systems, Adv. Intell. Syst. (2022) 2200001.

[10] T. Dalgaty, N. Castellani, C. Turck, et al., In situ learning using intrinsic memristor variability via Markov chain Monte Carlo sampling, Nat. Electron. 4 (2021) 151–161.

[11] R. Romero-Zaliz, E. Perez, F. Jiménez-Molinos, C. Wenger, J.B. Roldán, Study of quantized hardware deep neural networks based on resistive switching devices, conventional versus convolutional approaches, Electronics 10 (2021) 346.

[12] P.A. Merolla, J.V. Arthur, R. Alvarez-Icaza, A.S. Cassidy, J. Sawada, F. Akopyan, B. L. Jackson, N. Imam, C. Guo, Y. Nakamura, B. Brezzo, I. Vo, S.K. Esser, R. Appuswamy, B. Taba, A. Amir, M.D. Flickner, W.P. Risk, R. Manohar, D. S. Modha, A million spiking-neuron integrated circuit with a scalable communication network and interface, Science 345 (2014) 668–673.

[13] F. Alibart, E. Zamanidoost, D.B. Strukov, Pattern classification by memristive crossbar circuits using ex situ and in situ training, Nat. Commun. 4 (2013) 2072.

[14] D. Sakellaropoulos, P. Bousoulas, G. Nikas, C. Arvanitis, E. Bagakis, D. Tsoukalas, Enhancing the synaptic properties of low-power and forming-free HfOx/TaOy/ HfOx resistive switching devices, Microelectron. Eng. 229 (2020) 111358.

[15] M. Prezioso, F. Merrikh-Bayat, B.D. Hoskins, G.C. Adam, K.K. Likharev, D. B. Strukov, Training and operation of an integrated neuromorphic network based on metal-oxide memristors, Nature 521 (2015) 61–64.

[16] S. Yu, H. Jiang, S. Huang, X. Peng, A. Lu, Computing-in-memory chips for deep learning: recent trends and prospects, IEEE Circ. Syst. Mag. (2021) 31–56.

[17] E. Pérez-Bosch, R. Romero-Zaliz, E. Pérez, M. Kalishettyhalli, J. Reuben, M. A. Schubert, F. Jiménez-Molinos, J.B. Roldán, C. Wenger, Toward reliable compact modeling of multilevel 1T-1R RRAM devices for neuromorphic systems, Electronics 10 (2021) 645.

[18] R. Romero-Zaliz, E. Pérez, F. Jiménez-Molinos, C. Wenger, J.B. Roldán, Influence of variability on the performance of HfO$_2$ memristor-based convolutional neural networks, Solid State Electron. 185 (2021) 108064.

[19] Z. Wei, et al., True random number generator using current difference based on a fractional stochastic model in 40-nm embedded ReRAM, in: 2016 IEEE International Electron Devices Meeting (IEDM), San Francisco, CA, 2016, pp. 4.8.1–4.8.4.

[20] R. Carboni, D. Ielmini, Stochastic memory devices for security and computing, Adv. Electron. Mater. 5 (2019) 1900198.

[21] M. Lanza, C. Wen, X. Li, T. Zanotti, F.M. Puglisi, Y. Shi, F. Saiz, A. Antidormi, S. Roche, W. Zheng, X. Liang, J. Hu, S. Duhm, K. Zhu, F. Hui, J.B. Roldan, B. Garrido, T. Wu, V. Chen, E. Pop, Advanced data encryption using two-dimensional materials, Adv. Mater. 2100185 (2021) 1–12.

[22] A. Chen, Utilizing the variability of resistive random access memory to implement reconfigurable physical unclonable functions, IEEE Electron Device Lett. 36 (2) (2015) 138–140. Feb.

[23] D. Ielmini, R. Waser, Resistive Switching: From Fundamentals of Nanoionic Redox Processes to Memristive Device Applications, Wiley-VCH, 2015.

[24] M.A. Villena, J.B. Roldán, F. Jiménez-Molinos, E. Miranda, J. Suñé, M. Lanza, SIM2RRAM: a physical model for RRAM devices simulation, J. Comput. Electron. 16 (2017) 1095–1120.

[25] M. Salinga, B. Kersting, I. Ronneberger, V.P. Jonnalagadda, X.T. Vu, M. Le Gallo, I. Giannopoulos, O. Cojocaru-Mirédin, R. Mazzarello, A. Sebastian, Monatomic phase change memory, Nat. Mater. 17 (2018) 681–685.

[26] A.V. Khvalkovskiy, D. Apalkov, S. Watts, R. Chepulskii, R.S. Beach, A. Ong, et al., Basic principles of STT-MRAM cell operation in memory arrays, J. Phys. D. Appl. Phys. 46 (2013) 139601.

[27] M. Trentzsch, et al., A 28nm HKMG super low power embedded NVM technology based on ferroelectric FETs, in: 2016 IEEE International Electron Devices Meeting (IEDM), 2016, pp. 11.5.1–11.5.4.

[28] M. von Witzleben, K. Fleck, C. Funck, B. Baumkötter, M. Zuric, A. Idt, T. Breuer, R. Waser, U. Böttger, S. Menzel, Investigation of the impact of high temperatures on the switching kinetics of redox-based resistive switching cells using a high-speed nanoheater, Adv. Electron. Mater. 3 (2017) 1700294.

[29] C. Funck, S. Menzel, Comprehensive model of electron conduction in oxide-based memristive devices, ACS Appl. Electron. Mater. 3 (2021) 3674–3692.

[30] D. Maldonado, C. Aguilera-Pedregosa, G. Vinuesa, H. García, S. Dueñas, H. Castán, S. Aldana, M.B. González, E. Moreno, F. Jiménez-Molinos, F. Campabadal, J. B. Roldán, An experimental and simulation study of the role of thermal effects on variability in TiN/Ti/HfO2/W resistive switching nonlinear devices, Chaos, Solitons Fractals 160 (2022) 112247.

[31] M. Lanza, R. Waser, D. Ielmini, J.J. Yang, L. Goux, J. Suñe, A.J. Kenyon, A. Mehonic, S. Spiga, V. Rana, S. Wiefels, S. Menzel, I. Valov, M.A. Villena, E. Miranda, X. Jing, F. Campabadal, M. Gonzalez, F. Aguirre, F. Palumbo, K. Zhu, J. B. Roldan, F.M. Puglisi, L. Larcher, T.-H. Hou, T. Prodromakis, Y. Yang, P. Huang, T. Wang, Y. Chai, K.L. Pey, N. Raghavan, S. Duenas, T. Wang, Q. Xia, S. Pazos, Standards for the characterization of endurance in resistive switching devices, ACS Nano 15 (2021) 17214–17231.

[32] C.-C. Chou, et al., A 22nm 96KX144 RRAM macro with a self-tracking reference and a low ripple charge pump to achieve a configurable read window and a wide operating voltage range, in: 2020 IEEE Symposium on VLSI Circuits, 2020, pp. 1–2.

[33] P. Jain, et al., 13.2 A 3.6Mb 10.1Mb/mm2 embedded non-volatile ReRAM macro in 22nm FinFET technology with adaptive forming/set/reset schemes yielding down to 0.5V with Sensing Time of 5ns at 0.7V, in: 2019 IEEE International Solid-State Circuits Conference - (ISSCC), 2019, pp. 212–214.

[34] S. Poblador, M.B. González, F. Campabadal, Investigation of the multilevel capability of TiN/Ti/HfO2/W resistive switching devices by sweep and pulse programming, Microelectron. Eng. 187-188 (2018) 148.

[35] H.S.P. Wong, H.Y. Lee, S.Yu.Y.-S. Chen, Y. Wu, P.-S. Chen, B. Lee, F.T. Chen, M.-J. Tsai, Metal-oxide RRAM, Proc. IEEE 100 (6) (2012). June.

[36] U. Russo, C. Cagli, A.-L. Lacaita, Filament conduction and reset mechanism in NiO-based resistive-switching memory (RRAM) devices, Trans. Electron. Dev. 56 (2) (2009) 186–192. February.

[37] M. Maestro, M.B. González, F. Jiménez-Molinos, E. Moreno, J.B. Roldán, F. Campabadal, Unipolar resistive switching behavior in Al2O3/HfO2 multilayer dielectric stacks: fabrication, characterization and simulation, Nanotechnology 31 (2020) 135202.

[38] E. Miranda, S. Kano, C. Dou, K. Kakushima, J. Suñé, H. Iwai, Nonlinear conductance quantization effects in CeOx/SiO2-based resistive switching devices, Appl. Phys. Lett. 101 (2012), 012910.

[39] F. Palumbo, S. Lombardo, M. Eizenberg, Physical mechanism of progressive breakdown in gate oxides, J. Appl. Phys. 115 (22) (2014) 224101.

[40] G. Bersuker, D.C. Gilmer, D. Veksler, P. Kirsch, L. Vandelli, A. Padovani, L. Larcher, K. McKenna, A. Shluger, V. Iglesias, M. Porti, M. Nafría, Metal oxide resistive memory switching mechanism based on conductive filament properties, J. Appl. Phys. 110 (2011) 124518.

[41] F. Hui, P. Liu, S.A. Hodge, T. Carey, C. Wen, F. Torrisi, D. Thanuja, L. Galhena, F. Tomarchio, Y. Lin, E. Moreno, J.B. Roldan, E. Koren, A.C. Ferrari, M. Lanza, In-situ observation of low-power nano-synaptic response in graphene oxide using conductive atomic force microscopy, Small 2101100 (2021) 1–8.

[42] E. Pérez, D. Maldonado, C. Acal, J.E. Ruiz-Castro, F.J. Alonso, A.M. Aguilera, F. Jiménez-Molinos, Ch. Wenger, J.B. Roldán, Analysis of the statistics of device-to-device and cycle-to-cycle variability in TiN/Ti/Al:HfO2/TiN RRAMs, Microelectron. Eng. 214 (2019) 104–109.

[43] A.N. Mikhaylov, D.V. Guseinov, A.I. Belov, D.S. Korolev, V.A. Shishmakova, M. N. Koryazhkina, D.O. Filatov, O.N. Gorshkov, D. Maldonado, F.J. Alonso, J. B. Roldán, A.V. Krichigin, N.V. Agudov, A.A. Dubkov, A. Carollo, B. Spagnolo, Stochastic resonance in a metal-oxide memristive device, Chaos, Solitons Fractals 144 (2021) 110723.

[44] S. Dirkmann, J. Kaiser, C. Wenger, T. Mussenbrock, Filament growth and resistive switching in hafnium oxide memristive devices, ACS Appl. Mater. Interfaces 10 (17) (2018) 14857–14868.

[45] J.B. Roldán, F.J. Alonso, A.M. Aguilera, D. Maldonado, M. Lanza, Time series statistical analysis: a powerful tool to evaluate the variability of resistive switching memories, J. Appl. Phys. 125 (2019) 174504.

[46] D.O. Filatov, D.V. Vrzheshch, O.V. Tabakov, A.S. Novikov, A.I. Belov, I.N. Antonov, V.V. Sharkov, M.N. Koryazhkina, A.N. Mikhaylov, O.N. Gorshkov, A.A. Dubkov, A. Carollo, B. Spagnolo, Noise-induced resistive switching in a memristor based on ZrO2(Y)/Ta2O5 stack, J. Stat. Mech. Theory Exp. (2019) 124026.

[47] J. Guy, G. Molas, P. Blaise, M. Bernard, A. Roule, G. Le Carval, V. Delaye, A. Toffoli, G. Ghibaudo, F. Clermidy, B. De Salvo, L. Perniola, Investigation of forming, SET, and data retention of conductive-bridge random-access memory for stack optimization, IEEE Trans. Electron Dev. 62 (11) (2015) 3482–3489.

[48] F.J. Alonso, D. Maldonado, A.M. Aguilera, J.B. Roldan, Memristor variability and stochastic physical properties modeling from a multivariate time series approach, Chaos, Solitons Fractals 143 (2021) 110461.

[49] I.A. Surazhevsky, V.A. Demin, A.I. Ilyasov, A.V. Emelyanov, K.E. Nikiruy, V. V. Rylkov, S.A. Shchanikov, I.A. Bordanov, S.A. Gerasimova, D.V. Guseinov, N. V. Malekhonova, D.A. Pavlov, A.I. Belov, A.N. Mikhaylov, V.B. Kazantsev, D. Valenti, B. Spagnolo, M.V. Kovalchuk, Noise-assisted persistence and recovery of memory state in a memristive spiking neuromorphic network, Chaos, Solitons Fractals 146 (2021) 110890.

[50] V. Agudov, A.V. Safonov, A.V. Krichigin, A.A. Kharcheva, A.A. Dubkov, D. Valenti, D.V. Guseinov, A.I. Belov, A.N. Mikhaylov, A. Carollo, B. Spagnolo, Nonstationary distributions and relaxation times in a stochastic model of memristor, J. Stat. Mech. 024003 (2020).

[51] J.B. Roldán, G. González-Cordero, R. Picos, E. Miranda, F. Palumbo, F. Jiménez-Molinos, E. Moreno, D. Maldonado, S.B. Baldomá, Moner Al Chawa, C. de Benito, S.G. Stavrinides, J. Suñé, L.O. Chua, On the thermal models for resistive random access memory circuit simulation, Nanomaterials 11 (2021) 1261.

[52] P. Chen, S. Yu, Compact modeling of RRAM devices and its applications in 1T1R and 1S1R Array design, IEEE Trans. Electron Dev. 62 (12) (2015) 4022–4028. Dec.

[53] S. Aldana, P. García-Fernández, R. Romero-Zaliz, M.B. González, F. Jiménez-Molinos, F. Gómez-Campos, F. Campabadal, J.B. Roldán, Resistive switching in HfO2 based valence change memories, a comprehensive 3D kinetic Monte Carlo approach, J. Phys. D. Appl. Phys. 53 (2020) 225106.

[54] P. Huang, X.Y. Liu, B. Chen, H.T. Li, Y.J. Wang, Y.X. Deng, K.L. Wei, L. Zeng, B. Gao, G. Du, X. Zhang, J.F. Kang, A physics-based compact model of metal-oxide-based RRAM DC and AC operations, IEEE Trans. Electron Dev. 60 (12) (2013) 4090–4097.

[55] P. Huang, D. Zhu, S. Chen, Z. Zhou, Z. Chen, B. Gao, J. Kang, Compact model of HfOX-based electronic synaptic devices for neuromorphic computing, IEEE Trans. Electron Dev. 64 (2) (2017) 614–621.

[56] M.A. Villena, M.B. González, F. Jiménez-Molinos, F. Campabadal, J.B. Roldán, J. Suñé, E. Romera, E. Miranda, Simulation of thermal reset transitions in resistive switching memories including quantum effects, J. Appl. Phys. 115 (2014) 214504.

[57] M.A. Villena, M.B. González, J.B. Roldán, F. Campabadal, F. Jiménez-Molinos, F. M. Gómez-Campos, J. Suñé, An in-depth study of thermal effects in reset transitions in HfO2 based RRAMs, Solid State Electron. 111 (2015) 47–51.

[58] S. Kim, C. Du, P. Sheridan, W. Ma, S. Choi, W.D. Lu, Experimental demonstration of a second-order memristor and its ability to biorealistically implement synaptic plasticity, Nano Lett. 15 (3) (2015) 2203–2211.

[59] S. Kumar, R.S. Williams, Z. Wang, Third-order nanocircuit elements for neuromorphic engineering, Nat. Cell Biol. 585 (2020) 518–523.

[60] D. Barrera, M.J. Ibáñez, F. Jiménez-Molinos, A.M. Roldán, J.B. Roldán, A spline quasi-interpolation-based method to obtain the reset voltage in resistive RAMs in the charge-flux domain, J. Comput. Appl. Math. 354 (2019) 326–333.

[61] M.J. Ibáñez, F. Jiménez-Molinos, J.B. Roldán, R. Yáñez, Estimation of the reset voltage in resistive RAMs using the charge-flux domain and a numerical method based on quasi-interpolation and discrete orthogonal polynomials, Math. Comput. Simul. 164 (2019) 120–130.

[62] J.E. Ruiz-Castro, C. Acal, A.M. Aguilera, J.B. Roldan, A complex model via phase-type distributions to study random telegraph noise in resistive memories, Mathematics 9 (2021) 390.

[63] M.J. Ibáñez, D. Barrera, D. Maldonado, R. Yáñez, J.B. Roldan, Non-uniform spline quasi-interpolation to extract the series resistance in resistive switching memristors for compact modeling purposes, Mathematics 9 (2021) 2159.

[64] D. Maldonado, F. Aguirre, G. González-Cordero, A.M. Roldán, M.B. González, F. Jiménez-Molinos, F. Campabadal, E. Miranda, J.B. Roldán, Experimental study of the series resistance effect and its impact on the compact modeling of the conduction characteristics of HfO2-based resistive switching memories, J. Appl. Phys. 130 (2021), 054503.

[65] D. Maldonado, M.B. González, F. Campabadal, F. Jiménez-Molinos, M. Moner Al Chawa, S.G. Stavrinides, J.B. Roldan, Rodrigo Picos, L.O. Chua, Experimental evaluation of the dynamic route map in the reset transition of memristive ReRAMs, Chaos, Solitons Fractals 139 (2020) 110288.

[66] I. Hossen, M.A. Anders, L. Wang, G.C. Adam, Data-driven RRAM device models using kriging interpolation, Sci. Rep. 12 (2022) 5963.

[67] J.E. Ruiz-Castro, C. Acal, D. Maldonado, J.B. Roldan, One cut-point phase-type distributions in reliability. An application to resistive random access memories, Mathematics 9 (2021) 2734.

[68] A. Ortiz-Conde, F.J. Garcia-Sanchez, J.J. Liou, A. Cerdeira, M. Estrada, Y. Yue, Review of recent MOSFET threshold voltage extraction methods, Microelectron. Reliab. 42 (2002) 583–596.

[69] A. Ortiz-Conde, A. Sucre-González, F. Zárate-Rincón, R. Torres-Torres, R.S. Murphy-Arteaga, J.J. Liou, F.J. García-Sánchez, A review of DC extraction methods for MOSFET series resistance and mobility degradation model parameters, Microelectron. Reliab. 69 (2017) 1–16.

[70] X. Wen-Bo, L. Wei-Qing, W. Hua-Ming, Z. Hua-Ming, Review of parameter extraction methods for single-diode model of solar cell, Acta Phys. Sin. 67 (19) (2018) 198801.

[71] S. Aldana, P. García-Fernández, A. Rodríguez-Fernández, R. Romero-Zaliz, M. B. González, F. Jiménez-Molinos, F. Campabadal, F. Gómez-Campos, J.B. Roldán, A 3D kinetic Monte Carlo simulation study of resistive switching processes in Ni/HfO₂/Si-n+−based RRAMs, J. Phys. D. Appl. Phys. 50 (2017) 335103.

[72] S. Menzel, B. Klopstra, C. Kügeler, U. Böttger, G. Staikov, R. Waser, A simulation model of resistive switching in electrochemical metallization memory cells (ECM), in: MRS Online Proceedings Library Archive 1160, 2009, pp. 101–106.

[73] S. Menzel, U. Böttger, R. Waser, Simulation of multilevel switching in electrochemical metallization memory cells, J. Appl. Phys. 111 (2012), 014501/1-5.

[74] L. Larcher, A. Padovani, L. Vandelli, A simulation framework for modeling charge transport and degradation in high-k stacks, J. Comput. Electron. 12 (4) (2013) 658–665.

[75] S. Aldana, J.B. Roldán, P. García-Fernández, J. Suñe, R. Romero-Zaliz, F. Jiménez-Molinos, S. Long, F. Gómez-Campos, M. Liu, An in-depth description of bipolar resistive switching in Cu/HfOx/Pt devices, a 3D kinetic Monte Carlo simulation approach, J. Appl. Phys. 123 (2018) 154501.

[76] S. Aldana, E. Pérez, F. Jimenez-Molinos, C. Wenger, J.B. Roldán, Kinetic Monte Carlo analysis of data retention in Al:HfO2-based resistive random access memories, Semicond. Sci. Technol. 35 (2020) 115012.

[77] M.B. Gonzalez, J.M. Rafí, O. Beldarrain, M. Zabala, F. Campabadal, Analysis of the switching variability in Ni/HfO₂-based RRAM devices, IEEE Trans. Dev. Mater. Reliab. 14 (2) (2014) 769–771.

[78] S. Poblador, M. Maestro-Izquierdo, M. Zabala, M.B. González, F. Campabadal, Methodology for the characterization and observation of filamentary spots in HfOₓ-based memristor devices, Microelectron. Eng. 223 (2020) 111232.

[79] G.A. Patterson, J. Suñé, E. Miranda, Voltage-driven hysteresis model for resistive switching: SPICE modeling and circuit applications, IEEE Trans. Comput. Aided Des. Integr. Circ. Syst. 36 (12) (2017) 2044–2051. Dec.

[80] D. Maldonado, S. Aldana, M.B. González, F. Jiménez-Molinos, M.J. Ibáñez, D. Barrera, F. Campabadal, J.B. Roldán, Variability estimation in resistive switching devices, a numerical and kinetic Monte Carlo perspective, Microelectron. Eng. 257 (2022) 111736.

[81] C. Acal, J.E. Ruiz-Castro, A.M. Aguilera, F. Jiménez-Molinos, J.B. Roldán, Phase-type distributions for studying variability in resistive memories, J. Comput. Appl. Math. 345 (2019) 23–32.

[82] J.E. Ruiz-Castro, C. Acal, A.M. Aguilera, M.C. Aguilera-Morillo, J.B. Roldán, Linear-phase-type probability modelling of functional PCA with applications to resistive memories, Math. Comput. Simul. 186 (2021) 71–79.

[83] S. Long, C. Cagli, D. Ielmini, M. Liu, J. Suñé, Analysis and modeing of resistive switching statistics, J. Appl. Phys. 111 (2012), 074508.

[84] R. Picos, J.B. Roldán, M.M. Al Chawa, P. García-Fernández, F. Jiménez-Molinos, E. García-Moreno, Semiempirical modeling of reset transitions in unipolar resistive-switching based memristors, Radioeng. J. 24 (2015) 420–424.

[85] S. Deshmukh, M. Muñoz Rojo, E. Yalon, S. Vaziri, C. Koroglu, R. Islam, R. A. Iglesias, K. Saraswat, E. Pop, Direct measurement of nanoscale filamentary hot spots in resistive memory devices, Sci. Adv. 8 (2022) eabk1514.

[86] V. Karpov, D. Niraula, I. Karpov, Thermodynamic analysis of conductive filaments, Appl. Phys. Lett. 109 (2016), 093501.

[87] D.J. Wouters, S. Menzel, J.A.J. Rupp, T. Hennen, R. Waser, On the Universality of the I–V Switching Characteristics in Non-Volatile and Volatile Resistive Switching Oxides, Faraday Discussions, The Royal Society of Chemistry, 2019, pp. 1359–6640.

[88] A. Fantini, D.J. Wouters, R. Degraeve, L. Goux, L. Pantisano, G. Kar, Y.-Y. Chen, B. Govoreanu, J.A. Kittl, L. Altimime, M. Jurczak, Intrinsic switching behavior in HfO2 RRAM by fast electrical measurements on novel 2R test structures, in: 4th IEEE International Memory Workshop, Milan, 2012, pp. 1–4.

[89] M.B. González, M. Maestro, F. Jiménez-Molinos, J.B. Roldán, F. Campabadal, Current transient response and role of the internal resistance in HfOx-based memristors, Appl. Phys. Lett. 117 (2020) 262902.

[90] X. Guan, S. Yu, H.-S. Philip Wong, A SPICE compact model of metal oxide resistive switching memory with variations, Electron Dev. Lett. IEEE 33 (10) (2012) 1405–1407. Oct.

[91] Z. Jiang, S. Yu, Y. Wu, J.H. Engel, X. Guan, H.S.P. Wong, Verilog-a compact model for oxide-based resistive random access memory, in: Simulation of Semiconductor Processes and Devices (SISPAD), 2014 International Conference on, 2014, pp. 41–44, 9–11 Sept.

[92] Z. Jiang, Y. Wu, S. Yu, Member, L. Yang, K. Song, Z. Karim, H.-S.P. Wong, A compact model for metal–oxide resistive random access memory with experiment verification, IEEE Trans. Electron Dev. 63 (5) (2016) 1884–1892. May.